

DYNAMICS OF ELASTO-VISCO-PLASTIC MATERIALS IN STRONG EXTENSION**G.Ioannou¹, S. Varchanis¹, Y.Dimakopoulos^{1,*}, J. Tsamopoulos¹**¹Department of Chemical Engineering, University of Patras, Patras, Greece(*dimako@chemeng.upatras.gr)**ABSTRACT**

In this work we examine the flow of elasto-visco-plastic materials in the optimized-shape cross-slot extensional rheometer^[1] (OSCER). The shape of this geometry has been optimized numerically in order to generate a wide region of homogeneous elongational flow. Haward et al.^[1] demonstrated experimentally using PEO solutions, that such an ideal flow can remain steady for a wide range of extension rates in the OSCER. Based on their results for viscoelastic materials in the OSCER, we study the dynamics of elasto-visco-plastic materials in this purely extensional flow field. Such an investigation of yield-stress materials in elongational flows is necessary as indicated by recent experiments of Zhang et al.^[2] In their work, noticeable differences have been revealed with respect to the extensional behavior of complex yield-stress materials (e.g. the ratio of the extension yield-stress to the shear yield-stress is larger, by a factor of 1.5, than expected from the standard theory). In order to investigate the dynamics of elasto-visco-plastic materials in strong extension, we have simulated the flow of a 0.08% Carbopol[®] -940 aqueous solution using the Saramito/Herschel-Bulkley constitutive equation^[3] in the OSCER geometry. Performing a wide-range parametric analysis of the dynamics of the flow, we determine when steady-state or oscillatory solutions arise. Surprisingly, we find that even at high extension rates the system can reach to a steady state at which strong extension dominates a wide region around the stagnation point. However, when the flow rate is furtherly increased, we identify a critical value of the flow rate that drives the system to a periodic state.

INTRODUCTION

The majority of people use many materials in their everyday life that are characterized as viscoplastic, such as toothpaste, butter, cosmetic creams etc. Not only in people's everyday life, but also in industry (e.g. concrete), environment (e.g. lava flow) and our bodies (e.g. mucus), viscoplastic materials are present^[4]. Although these materials are very common, they had not received attention for years. The common feature of the examples mentioned is their ability to flow when high stresses are applied; on the contrary their behavior is solid-like at low stresses. The most convenient way to describe the transition is by introducing the term of yield stress, τ_y , which causes these fluids to be called yield stress fluids.

Almost a century has passed since Bingham described these materials (1922) with a simple model, which assumes that the material responds as a Newtonian fluid when it is found in a yielded state, and as a rigid solid when it is found in an unyielded state. A recent model introduced by Saramito^[3], describes such materials as elastic solids when found in an unyielded state and as viscoelastic fluids when found in a yielded state. These materials are called elasto-visco-plastic (EVP). Some examples of this type of fluids are emulsions, liquid foams and Carbopol gel.

The development of constitutive equations is a very challenging procedure. There is no generally accepted model for yield stress fluids, in contrast to polymeric fluids whose behavior can be predicted in any type of flow. This happens because single-phase materials and especially polymer solutions and polymer melts have attracted mainly the research interest in the past decades, resulting to the development of robust and accurate constitutive equations. Consequently, many efforts have been made to establish appropriate EVP constitutive equations based on principles that govern the response of polymeric fluids. The most common way for validating possible models is by

comparison of the predictions of the model to experimental measurements of the stresses. While shear stresses are easy to measure with the use of rotational rheometers, the measurement of normal stresses is extremely difficult^[5] due to various factors such as: heterogeneity of the flow, residual stresses and instrument sensitivity. In addition, producing a shear-free flow field is a great challenge.

Cross-slot rheometers consist of perpendicular, bisecting channels with inlets and outlets that cause a stagnation point at the center of symmetry. They are often used because of their ability to generate a stagnation point, at which the fluid velocity is zero, in contrast to the velocity gradient. This means that at this particular point planar elongational flow is generated. Many studies, both experimental^[6] and computational^[7], have examined the flow of viscoelastic materials in the cross-slot geometry by examining the dynamics of the flow. It has been found^[6,8] that elastic instabilities occur after a critical value of flow rate, which lead to flow asymmetry and unsteady flow. Additionally, in the standard cross-slot device the region where purely elongational flow is generated is quite limited, due to the sharpness of the cross-slot corners. Therefore, the extension rate is well-defined only at the stagnation point. Even when Cruz et al.^[7] attempted to reduce the sharpness of the corners, and in turn the influence of shear, by rounding the corners, the dynamics of this flow did not change dramatically. Thus, Alves^[9] introduced a new optimized shaped cross-slot rheometer (OSCER), which has the ability to create a wider region of planar elongational flow. Alves^[9] suggested that this numerically optimized geometry can generate a steady shear-free velocity field insensitive to inertial and elastic instabilities. Haward et al.^[1] validated this assumption by performing experiments with dilute PEO solutions and illustrating that a symmetric steady flow field can be maintained in the OSCER even at very high extension rates. The OSCER geometry resembles a standard cross-slot device, in which the corners have been pulled from the opposite direction, being salient and forming a square in the center of the device. In the corners of the OSCER, fluid is trapped causing self-lubrication of the flow and creating a shear-free domain with purely elongational flow. While EVP fluids have never been tested in this geometry, experiments with viscoelastic fluids^[1] indicate that this rheometer has many capabilities. Thus, in this study we investigate the potential of using the optimized cross-slot device as an instrument for measuring the normal stresses and quantifying the extensional response of complex yield-stress fluids.

PROBLEM FORMULATION

The creation of the OSCER geometry, which is used in this work, is determined using Fig. 1 from the work of Haward et al.^[10]. The data points of the walls of the device are extracted from a digitized photograph of the OSCER. Then using the Software Eureka^[11,12], and taking advantage of the symmetry of OSCER, we found the equation that best fits the points that correspond to the one eighth of the geometry. The result of this equation, rotated by -45 degrees, can be seen in Fig. 1 (b) (red color), and the final geometry of the OSCER can be seen in Fig. 1 (a).

The four channels of the OSCER have a width equal to $W = 200 \mu\text{m}$. The distance from inflow and outflow boundaries to the center of the cross-slot, L , is equal to $20.5*W$. This length has been found to be adequate in retaining a fully developed flow at the inflow and outflow boundaries during flow simulations. We assume two-dimensional flow, considering that the OSCER is very deep in the third dimension, perpendicular to the xy plane. The inlet channels, from where the fluid enters the rheometer, are parallel to the y -axis and the outlet channels are parallel to the x -axis (see Fig. 1). Note that in Fig. 1 (a), \tilde{L} and \tilde{W} are in scale. We have validated our geometry, by solving the momentum and mass conservation for DOP, a Newtonian fluid, and comparing our results to the experimental ones reported by Haward et al.^[10].

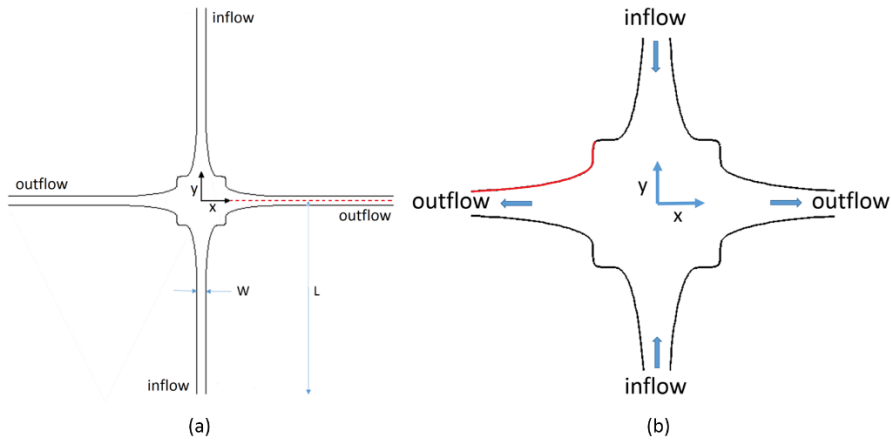


Figure 1. The OSCER geometry. (a) The whole rheometer, (b) Zoom in the center of the cross-slot.

In order to get an estimation for the values of the material parameters of the constitutive model, we fit the SRM/HB model to the experimental data of Putz et al.^[13]. The material of interest is a 0.08% Carbopol solution. We estimate the elastic modulus \tilde{G} , from LAOS data, and we fit the rest of parameters, namely, the yield stress $\tilde{\tau}_y$, the consistency parameter \tilde{K} and the HB exponent n to the flow curve. For this material, we estimate the elastic modulus $\tilde{G} = 62.5 Pa$, the consistency parameter $\tilde{K} = 4.838 Pa s^n$, the yield stress $\tilde{\tau}_y = 1.67 Pa$ and the power index $n = 0.332$. The scaling quantities for the non-dimensionalization of the governing equations are the width of the channel \tilde{W} , the characteristic mean velocity at the inflow \tilde{U} , the characteristic time of the flow \tilde{W}/\tilde{U} , the characteristic time of the material $(\tilde{K}/\tilde{G})^{1/n}$ and the characteristic stress \tilde{G} . We also define the Reynolds (Re), Weissenberg (Wi), yield strain (ε_y) and Bingham, (Bn) dimensionless numbers as follows:

$$Re = \frac{\tilde{\rho}\tilde{U}^2}{\tilde{G}} \quad (1)$$

$$Wi = \frac{\text{material's characteristic time}}{\text{flow's characteristic time}} = \frac{(\tilde{K}/\tilde{G})^{1/n}\tilde{U}}{\tilde{W}} \quad (2)$$

$$\varepsilon_y = \frac{\tilde{\tau}_y}{\tilde{G}} \quad (3)$$

$$Bn = \frac{\varepsilon_y}{Wi} \quad (4)$$

where $\tilde{\rho}$ is the Carbopol gel's density.

Note that the quantities that feature a tilde are dimensional; otherwise the quantities are dimensionless. The 2-dimensional flow in the OSCER is governed by the laws of continuity (5) and momentum conservation (6):

$$\nabla \cdot \mathbf{u} = 0 \quad (5)$$

$$Re \left(\frac{\partial \mathbf{u}}{\partial t} + \mathbf{u} \cdot \nabla \mathbf{u} \right) + \nabla \cdot (p\mathbf{I}) - \nabla \cdot \boldsymbol{\tau} = \mathbf{0} \quad (6)$$

where \mathbf{u} is the velocity vector, p the thermodynamic pressure, \mathbf{I} the identity tensor, and $\boldsymbol{\tau}$ the extra stress tensor. In the equation (6), there is no gravity term, because we assume that the action of gravity is in the third dimension and does not affect the flow. Also, creeping flow is assumed ($Re=0$), so that Eq. (6) can be written as:

$$\nabla \cdot (p\mathbf{I}) - \nabla \cdot \boldsymbol{\tau} = \mathbf{0} \quad (7)$$

The constitutive model, which is used in this work is the so called Saramito/Herschel-Bulkley model^[3], which can be written in its dimensionless form as:

$$\nabla \cdot \boldsymbol{\tau} + \max \left(0, \frac{|\boldsymbol{\tau}_D| - \varepsilon_y}{|\boldsymbol{\tau}_D|^n} \right) \frac{1}{n} \frac{\boldsymbol{\tau}}{Wi} = \dot{\boldsymbol{\varepsilon}} \quad (8)$$

Where $\boldsymbol{\tau}_D = \boldsymbol{\tau} - \frac{1}{3} \text{tr}(\boldsymbol{\tau})\mathbf{I}$ denotes the deviatoric part of $\boldsymbol{\tau}$. We also denote as $\dot{\boldsymbol{\varepsilon}} = \nabla \mathbf{u} + (\nabla \mathbf{u})^T$ the rate of deformation tensor and as $\overset{\nabla}{\boldsymbol{\tau}} = \frac{\partial \boldsymbol{\tau}}{\partial t} + \mathbf{u} \cdot \nabla \boldsymbol{\tau} - (\nabla \mathbf{u})^T \cdot \boldsymbol{\tau} - \boldsymbol{\tau} \cdot (\nabla \mathbf{u})$ the upper-convected time derivative of the stress tensor.

We solve the mass (5) and momentum conservation (7) coupled with the constitutive Eq. (8) in the OSCER flow geometry. With respect to boundary conditions, we impose the no slip and no penetration conditions on the channel walls:

$$\mathbf{u} = \mathbf{0} \quad (9)$$

Additionally, boundary conditions must be applied at the entrance and exit of the channels. At the inflow, we impose one-dimensional equations which are solved together with the two-dimensional equations for the rest of the domain. We impose the following flow rate for steady one-dimensional flow for the inflow boundary at $y = L$ and $y = -L$, respectively.

$$Q = \int_0^W u_y|_{y=L} dx = -(1 - e^{-t}) \quad (10.a)$$

$$Q = \int_0^W u_y|_{y=-L} dx = (1 - e^{-t}) \quad (10.b)$$

This flow rate causes a constant pressure gradient $\Delta p / \Delta y$. When simulating the transient flow, at each time step we solve the one-dimensional equations under the respective constant pressure gradient. Along the outflow boundaries we apply the open boundary condition (OBC)^[14]. In this way we eliminate any numerical error that could arise due to the truncation of the domain. Using this particular boundary condition, we do not impose the fluid velocity and stresses, but we calculate them from the weak form of the governing equations. The governing equations are solved numerically using the newly proposed stabilized finite element method by Varchanis et al.^[15] that features equal order interpolation of all variables (velocities/pressure/stresses) and makes use of the log-conformation representation of the constitutive equation. The domain is discretized in triangular elements using the quasi-elliptic mesh generator proposed by Dimakopoulos and Tsamopoulos^[16]. Finally, fully implicit transient simulations are performed in order to investigate and understand the nonlinear dynamics of this stagnation point flow.

RESULTS AND DISCUSSION

Before we proceed to the discussion of the results, it is useful to define the local Wi and Bn numbers, which are based on the deformation rate at the stagnation point. We define as Wi_{sp} the local Weissenberg number at the stagnation point:

$$Wi_{sp} = Wi \dot{\varepsilon} \quad (11)$$

Where $\dot{\varepsilon} = |\partial u_x / \partial x|$ is the rate of deformation at the stagnation point. From the definition of Eq. (4) for the Bingham number, the local Bingham number at the stagnation point is given as:

$$Bn_{sp} = \frac{\varepsilon_y}{Wi_{sp}} \quad (12)$$

Initially we will examine the EVP flow in the OSCER. Fig. 2 presents the predicted steady first normal stress difference ($\tau_{xx} - \tau_{yy}$), which is denoted as N_1 , as a function of the Wi_{sp} number at the stagnation point. At the upper axis of the figure, we present the respective local Bingham number Bi_{sp} . Starting from very low values of the flow rate, we can observe that N_1 forms a plateau. This plateau resembles the plateau at simple shear flow experiments, and defines a yield normal stress. This observation gives the opportunity to determine the value of the normal yield stress through the OSCER device.

Fig. 3 depicts close-ups of the OSCER device at certain local Wi_{sp} numbers, which are marked as red crosses in Fig. 2. At the left part of each close-up we present the streamlines of the flow, superimposed on the yield surfaces. In the regions of the geometry that are red, the material is in a yielded state, while in the regions of the geometry that are blue, the material is in an unyielded state. At the right part of the close-ups we present the contours of N_1 .

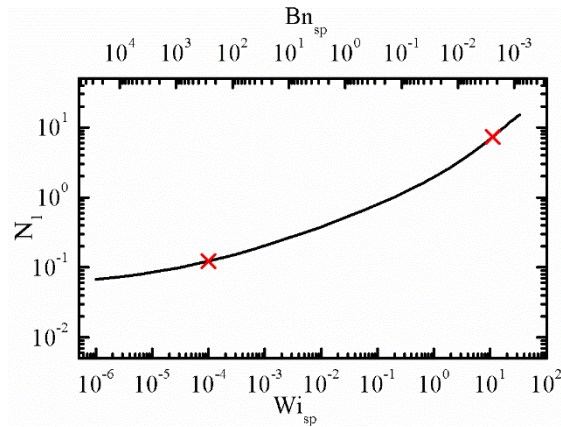


Figure 2. First normal stress difference, N_1 , at the stagnation point versus Wi_{sp} and Bn_{sp} .

In Fig. 3 it is evident from the contours of N_1 that a large area of homogeneous extensional flow is generated around the stagnation point. Examining the close-ups of the OSCER for low flow rates, we can observe that unyielded regions exist close to the stagnation point and at the salient corners of the OSCER. With increasing flow rate, the unyielded regions vanish and the flow enters a viscoelastic regime. The material particles become more and more stretched in the x-direction and the streamlines feature a bending shape close to the stagnation point, something that is a clear sign of viscoelasticity. Similar streamlines and N_1 profiles have been observed in the viscoelastic fluid experiments^[10]. In Fig. 3 (a) unyielded regions are detected at the salient corners of the OSCER, where the velocity is almost zero, and also at a place between the stagnation point and the corner, where the velocity is not zero. In the unyielded regions it holds that $|\tau_D| < \varepsilon_y$, which means that the tension required to yield is not posed on the material and thus it remains solid.

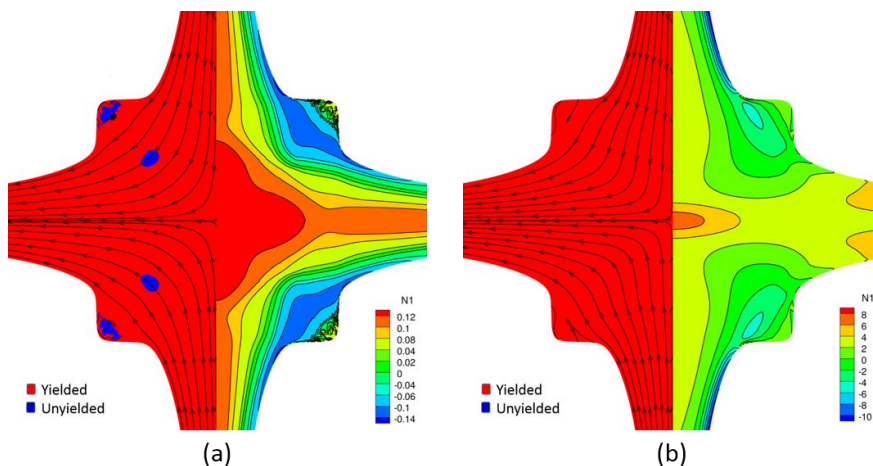


Figure 3. Yielded/unyielded regions along with streamlines on the left hand side and contours of the first normal stress difference, N_1 , on the right hand side for $Wi_{sp} = 10^{-4}$ (a) and $Wi_{sp} = 10$ (b).

For Wi_{sp} numbers greater than 34, the flow ceases to be steady and symmetric and becomes periodic and asymmetric. In Fig. 4 we present the first normal stress difference versus time for $Wi_{sp} = 40$. In order to observe some details in the periodic solution we additionally present Fig. 4 (b) which is a magnification of the temporal evolution of N_1 inside the red circle of Fig. 4 (a). In Fig. 4 (b)

we can observe the startup of the periodic solution as well as the amplitude of the periodic oscillation of N_I at the stagnation point. The period of the phenomenon is determined to be equal to 4.68.

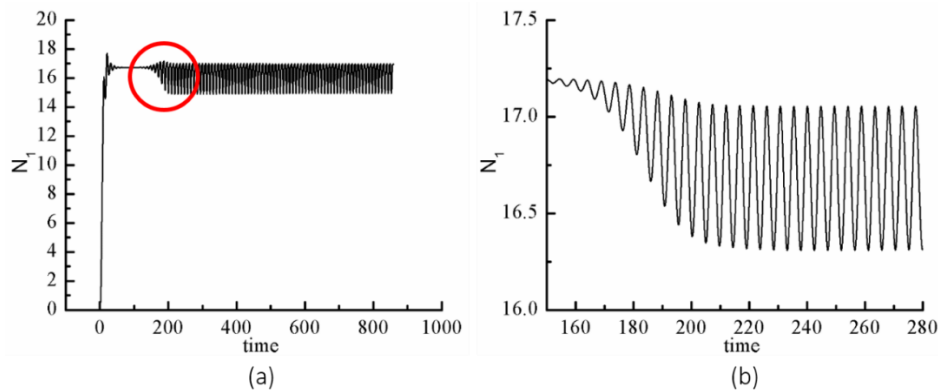


Figure 4. (a) First normal stress difference versus time for the base case at $Wi_{sp} = 40$, (b) zoom in at the time when periodic solution arises.

CONCLUSIONS

We have examined the flow of a 0.08% Carbopol[®] -940 aqueous solution in the OSCER. This rheometer generates a wide flow field that produces pure elongational flow, in contrast to the standard cross-slot rheometer which generates elongational flow only at the stagnation point. We have solved the momentum and mass conservation equations coupled with the Saramito/Herschel-Bulkley constitutive equation using the in-house stabilized Finite Element Solver of our lab. Our results indicate that at low flow rates, elastoplastic effects can be detected and the yield normal stress can be measured, while at high flow rates, viscoelastic effects can be evaluated. For a wide range of extension rates, a symmetric steady flow is established. Nevertheless, in all cases we find a critical value at which transient instabilities arise and the apparatus cannot give accurate results.

REFERENCES

- [1] S.J. Haward, M.S.N. Oliveira, M.A. Alves, G.H. McKinley. PRL, 109 (2012) 128301
- [2] X. Zhang, O. Fadoul, E. Lorenceau, and P. Coussot. PRL, 120 (2018) 048001
- [3] P. Saramito. J. Non-Newt. Fluid Mech., 158 (2009) 154-161.
- [4] N.J Balmforth., I.A. Frigaard, and G. Ovarlez. Annual Review of Fluid Mechanics 46 (2014) 121-46
- [5] H. De Cagny, M. Fazilati, M. Habibi, M. M. Denn, and D. Bonn. JOR 63 (2019) 285
- [6] P. E. Arratia, C. C Thomas, J. Diorio and J.P. Gollub. PRL 96 (2006) 144502
- [7] F.A. Cruz, R.J. Poole, A.M. Afonso, F.T. Pinho, P.J. Oliveira, M.A. Alves. JNNFM 214 (2014) 57-68
- [8] R. J. Poole, M. A. Alves, and P. J. Oliveira. Phys. Rev. Lett. 99 (2007) 164503
- [9] M.A. Alves. The XVth International Congress on Rheology, The Society of Rheology 80th Annual Meeting, American Institute of Physics 978-0-7354-0549-3/2008
- [10] S.J. Haward. Biomicrofluidics 10 (2016) 043401
- [11] M. Schmidt, H. Lipson. Eureka (Version 0.98 beta) (2014) [Software].www.nutonian.com
- [12] M. Schmidt, H. Lipson. Science, 324:5923 (2009) 081 – 85
- [13] A. M. V. Putz, T. I. Burghelca, I. A. Frigaard and D. M. Martinez. Phys. Fluids 20 (2008) 033102
- [14] T.C. Papanastasiou, N. Malamataris, K. Ellwood. Int. J. Numer. Methods Fluids 14 (1992) 587-608
- [15] S.Varchanis, A. Syrakos, Y. Dimakopoulos, J. Tsamopoulos. JNNFM 267 (2019) 78-97
- [16] Y. Dimakopoulos, J. Tsamopoulos. J. Comp. phys. 192 (2003) 494-522